Supramolecular architectures in luminescent Zn(II) and Cd(II) complexes containing imidazole derivatives: Crystal structures, vibrational and thermal properties, Hirshfeld surface analysis and electrostatic potentials

CrossMark

Alejandro Di Santo [a], Gustavo A. Echeverría [b, 1], Oscar E. Piro [b, 1], Hiram Pérez [c, **], Aida Ben Altabef [a, ***, 1], Diego M. Gil [a, *, 1]

[a] INQUINOA (CONICET-UNT), Instituto de Química Física, Facultad de Bioquímica, Química y Farmacia, Universidad Nacional de Tucumán, San Lorenzo 456, T4000CAN, San Miguel de Tucumán, Argentina
[b] Departamento de Física, Facultad de Ciencias Exactas, Universidad Nacional de La Plata, Institute IFLP (CONICET, CCT-La Plata), C.C. 67, 1900, La Plata, Argentina
[c] Departamento de Química Inorgánica, Facultad de Química, Universidad de La Habana, Habana, 10400, Cuba

A R T I C L E   I N F O

A B S T R A C T

Three novel zinc and cadmium complexes with 1-methylimidazole and 2-methylimidazole as ligands, mono-nuclear dichloro-bis(1-methylimidazole) zinc(II) and dibromo-bis(2-methylimidazole)cadmium(II) monohydrate complexes, and poly-nuclear bis(1-methylimidazole)-di-(μ2-bromo)cadmium(II) complex, namely, compounds 1–3, respectively, have been synthesized. The complexes were characterized by IR and Raman spectroscopies, thermal analysis and fluorescence. All the compounds exhibit interesting luminescent properties in solid state originated from intra-ligand ($\pi \rightarrow \pi^*$) transitions. Crystal structures of 1–3 were determined by single-crystal X-ray diffraction. Compound 1 crystallizes in $P2_1/n$ space group, the Zn(II) ion lies at a crystal general position in a tetrahedral environment, and the mono-nuclear units are weakly bonded to one another by C–H···Cl hydrogen bonds. Compound 2 crystallizes in Pnma space group, and mirror-related tetrahedral units around Cd(II) ion are H-bonded through a water molecule. Compound 3 crystallizes in $P2_1/c$ space group, and the Cd(II) ion presents a centrosymmetric octahedral coordination. Neighboring and equatorial edge-sharing octahedra conform a polymeric arrangement that extends along the crystal a-axis. Weak hydrogen bonds are the major driving forces in the crystal packing of the three complexes. Hirshfeld surface analysis reveals a detailed scrutiny of intermolecular interactions experienced by each complex. The surfaces mapped over d_{norm} property highlight the X···H (X = Cl, Br) as the main intermolecular contacts for the three complexes, being also relevant the presence of O···H contacts for complex 2. The surfaces mapped over Shape index and curvedness properties for the two Cd complexes allow identify $\pi \cdots \pi$ stacking interactions which are absent in the Zn complex. 2D fingerprint plots have been used to quantify the relative contribution of the intermolecular contacts to crystal stability of compounds, showing the crucial importance of weak interactions in building different supramolecular architectures. Furthermore, molecular electrostatic potentials for visualizing and quantifying the attractive character of interactions were calculated.

1. Introduction

The design and construction of coordination polymers are attracting considerable attention due to their structural diversities and potential applications including luminescence [1,2], chemical sensors [3,4], ion exchange [5], molecular magnetism [6,7], and heterogeneous catalysis [8–10]. It is difficult to predict the final

* Corresponding author.
** Corresponding author.
*** Corresponding author.
   E-mail addresses: hperez@fq.uh.cu (H. Pérez), altabef@fbqf.unt.edu.ar (A. Ben Altabef), dmgil@fbqf.unt.edu.ar (D.M. Gil).
[1] Members of the Research Career of CONICET.

structures of coordination polymers since many factors, such as the different conformation of organic ligands, solvent systems, metal ions, the auxiliary coligands, and temperature, are found to greatly influence the required structures [11,12]. Of the Zn(II) and Cd(II) d^{10} metal ions, the latter is larger in size and exhibits a variety of coordination geometries and coordination numbers. This behavior is due to its border line acidity and Cd(II) can coordinate both the soft and hard centers of organic blockers. As a result, the use of different organic blockers improves the design and synthesis of Cd(II)-based polymeric compounds with potential utility in the field of crystal engineering [13,14]. Actually, the geometry of cadmium complexes results from a balance between the bonding energies and repulsion amongst ligands [15].

The presence of coordination spacers such as halogens (Cl, Br, I) or ligands like N_3^- or SCN^- in the coordination compounds are capable of modifying the coordination pattern, the geometry and stereochemistry of the resulting compounds. The use of organic ligands such as the heterocycle N-donor molecules (e.g. imidazole, pyrazole, thiazole and their derivatives) modulates the construction and the dimension of the polymeric coordination network [16].

In the last years, various advances in crystal engineering of supramolecular architectures have been reported [17], being relevant in the identification and understanding of non-covalent intermolecular interactions. It is well known that such interactions are crucial in the control of the structures and properties of molecular assemblies of liquids, molecular crystals and biological molecules [18]. Besides the classical and strong hydrogen bonds, other weaker non-covalent interactions such as $C-H\cdots X$ (X = halogens, O, N) [19], π-π stacking [20] and $C-H\cdots\pi$ [21] interactions have shown to be very important in the crystal stabilization of transition metal complexes.

The studies of imidazole and its derivatives are very interesting taking into account their biological importance due to their presence in the structures of nucleic acids bases adenine and guanine and in the aminoacid histidine. Various metal complexes with imidazole as ligand have been used as models of metalo proteins [22,23]. In the early studies, metal complexes with imidazole and its derivatives were described in literature [24—30]. Lee et al. have studied a series of Zn(II) complexes with N-alkyl substituted imidazoles with crystal liquid behaviour upon cooling [28]. Abuskhuna and co-workers [26] have reported the synthesis and structural characterization of mononuclear Mn(II), Cu(II) and Zn(II) metal complexes with bis(imidazol-2-yl)methane (2-BIM) and its derivatives. These ligands have great interest because they can mimic multi-histidine coordination in biological systems [31]. In these complexes, the Zn(II) ion has a significantly distorted geometry from regular tetrahedral. The 2D structures of these compounds are stabilized by hydrogen bonds between the perchlorate anion and the amine group of the 2-BIM derivatives. Similar results were observed for the mononuclear metal complex between Zn(II) and 2-(1-hydroxy-4,5-dimethyl-1H-imidazol-2-yl)pyridine as ligand [27]. The most important results obtained for this compound is the significant increase in the luminescence intensity of Zn(II) complexes compared with the weakly luminescenting ligands in solid state [27].

In this contribution, we report the synthesis, thermal analysis, spectroscopic characterization and structural study by X-ray diffraction of three metal complexes with imidazole derivatives as ligands. A detailed analysis of intermolecular interactions by Hirshfeld surfaces computational method of the mono-nuclear dichloro-bis (1-methylimidazole) zinc(II) and dibromo-bis (2-methylimidazole) cadmium(II) monohydrate complexes, as well as the poly-nuclear bis (1-methylimidazole)-di-(μ2-bromo)cadmium(II) complex, namely, compounds **1**—**3**, respectively, was performed. The Hirshfeld surfaces are mapped with d_{norm}, *shape-*

index and *curvedness* properties [32—35] in order to analyze packing features. 2D-fingerprint plots enable us to decode and quantify the intermolecular interaction types present in the three crystal structures. By the other side, the molecular electrostatic potential (ESP) maps [36—38] allow visualize and estimate the electrostatic nature of interactions, existing also a direct relationship between electrostatic potential and reactivity of the molecules [39]. Electrophilic and nucleophilic regions are easily visualized through the electrostatic characterization of the chemical species, and therefore can be useful for the chemical activity prediction. In addition, molecular electrostatic potential constitutes an effective magnitude for analyzing and predicting noncovalent interactions [40—43].

2. Experimental

2.1. General procedures

All the reagents and solvents used in this work were purchased commercially and were used without further purification.

2.1.1. Methods and instrumentation

Elemental analysis (carbon, hydrogen and nitrogen) were performed using a Carlo Erba 1108 analyzer. Infrared absorption spectra in KBr pellets (4000-400 cm^{-1}) were recorded using a Perkin Elmer GX1 FTIR instrument. The Raman dispersion of the complexes in the solid state was measured in the spectral range from 3500 to 50 cm^{-1} with a Thermoscientific DXR Raman microscope. The Raman data were collected using a diode-pump, solid state laser of 532 nm wavelength (at 5 cm^{-1} spectral resolution), a confocal aperture of 25 μm pinhole, and a 10× objective. Thermogravimetric (TGA) and differential thermal analysis (DTA) measurements were performed with a Shimadzu DTG-60 thermobalance in the temperature range from 25 to 800 °C at a heating rate of 5°/min under air flow. Fluorescence spectra of the complexes were recorded in the solid state with a luminescence Perkin-Elmer LS-55 spectrometer.

2.1.2. Synthesis of complexes
2.1.2.1. *Synthesis of ZnL_2Cl_2 (1).* A solution of $ZnCl_2$ (1 mmol) in water (10 mL) was added dropwise to a water solution of 1-methylimidazole (2 mmol). The mixture was stirred for 2 h and the formed precipitate was filtered. Colourless single crystals were obtained by slow solvent evaporation from the filtrate after a few days. Yield 60%. *Anal.* Calc. for $C_8H_{12}Cl_4N_4Zn$: C, 25.85; H, 3.23; N, 15.07. Found: C, 25.78; H, 3.25; N, 14.98%.

2.1.2.2. *Synthesis of $[CdL'_2Br_2]\cdot H_2O$ (2).* It was synthesized by mixing aqueous solutions of cadmium (II) bromide (1 mmol) and 2-methylimidazole (2 mmol). Colorless single crystals were obtained by slow solvent evaporation after two days. Yield 75%. *Anal.* Calc. for $C_8H_{14}Br_2CdN_4O$: C, 21.12; H, 3.08; N, 12.32. Found: C, 21.09; H, 3.06; N, 12.29%

2.1.2.3. *Synthesis of $[CdL_2Br_2]_n$ (3).* A water solutions of cadmium (II) bromide (1 mmol) and 1-methylimidazole (2 mmol) were slowly added together. The resulting mixture was stirred for 1 h. Colorless crystals suitable for structural analysis were obtained after one day. Yield 92%. *Anal.* Calc. for $C_8H_{12}Br_2CdN_4$: C, 21.99; H, 2.75; N, 12.83. Found: C, 22.02; H, 2.78; N, 12.78%

2.1.3. X-ray diffraction data
The measurements were performed on an Oxford Xcalibur, Eos, Gemini CCD diffractometer with graphite-monochromated MoKα (λ = 0.7107 Å) radiation. All diffraction experiments were carried out at 293 K. X-ray diffraction intensities were collected (ω scans

with ϑ and κ-offsets), integrated and scaled with CrysAlisPro [44] suite of programs. The unit cell parameters were obtained by least-squares refinement (based on the angular settings for all collected reflections with intensities larger than seven times the standard deviation of measurement errors) using CrysAlisPro. Data were corrected empirically for absorption employing the multi-scan method implemented in CrysAlisPro.

The structures were solved with the intrinsic phasing procedure implemented in SHELXT of the SHELX suite of programs [45]. The molecular models were refined by full-matrix least-squares procedure with SHELXL of the same package.

2.1.3.1. [ZnL₂Cl₂]. All H-atoms were refined with the riding model.

2.1.3.2. [CdL′₂Br₂]·H₂O. All the water hydrogen atoms were refined with the riding model. The water H-toms were located in a difference Fourier map and refined at their found positions by restraining Ow-H and H⋯H distances to 0.86(1) and 1.36(1) Å, with an isotropic displacement parameter equal to 1.5 times the one of the water oxygen.

2.1.3.3. [CdL₂Br₂]ₙ. The aromatic H-atoms of methylimidazole were located in a difference Fourier map and refined at their found positions with isotropic displacement parameters. The methyl H-atoms were positioned on stereo-chemical basis and refined with the riding model as rigid groups allowed to rotate around their corresponding N–C bond such as to maximize the sum of the observed residual electron density at their calculated positions. As a result the –CH₃ group converged to staggered conformation.

Crystal data, data collection procedure, and refinement results for all three complexes are summarized in Table 1. Full crystallographic data have been deposited at the Cambridge Crystallographic Data Centre (CCDC 1472472–1472474). Enquiries for data can be direct to: Cambridge Crystallographic Data Centre, 12 Union Road, Cambridge, UK, CB2 1EZ or (e-mail) deposit@ccdc.cam.ac.uk or (fax) +44 (0) 1223 336033.

The geometry of the molecules was calculated using the WinGX [46] and Platon for Windows Taskbar v1.17 [47] softwares. ORTEP-3 [48] and Mercury [49] programs were used for molecular graphics.

2.1.4. Hirshfeld surface calculations

Hirshfeld surfaces and their associated two-dimensional fingerprint plots [32–35] were drawn by using CrystalExplorer3.0 software [50]. The d_{norm} (normalized contact distance) surface and the break down of two-dimensional fingerprint plots were used for decoding and quantifying intermolecular interactions in the crystal lattice. The d_{norm} is a symmetric function of distances to the surface from nuclei inside and outside the Hirshfeld surface (d_i and d_e, respectively), relative to their respective Van der Waals radii. 3D d_{norm} surfaces are mapped over a fixed color scale of −0.079 a.u. (red) − 0.722 Å a.u. (blue), *Shape index* mapped in the color range of −1.0 a.u. (concave) −1.0 a.u. (convex) Å, and *Curvedness* in the range of −4.0 a.u. (flat) − 0.01 a.u. (singular) Å. The 2D fingerprint plot displayed by using the translated 0.6–2.6 Å range, and including reciprocal contacts.

Molecular electrostatic potentials mapped over electron density distribution on 0.008 e Å⁻³ isosurfaces are calculated at the Hartree-Fock level by using of Tonto program [51] integrated into *CrystalExplorer*. The 6-31G* and STO-3G basis sets were used for Zn(II) and Cd(II) complexes, respectively.

3. Results and discussion

3.1. Vibrational study

FTIR and Raman spectroscopy were employed to confirm the presence of the functional groups in the crystal and also to investigate their vibrational behavior. The IR and Raman spectra of the 1-methylimidazole and its Zn(II) and Cd(II) complexes are shown in Fig. S1 and the corresponding ones for 2-methylimidazole and its Cd(II) complexes are shown in Fig. S2. The Raman spectra of the ligands and complexes are shown in Fig. S3 and S4. The characteristic vibrational modes of the metal complexes were compared to those of similar materials and to the vibrational assignment of 1-methylimidazole and 2-methylimidazole [52,53].

In complex **2**, the strong absorption bands observed in the IR

Table 1
Crystal data and structure refinement for compounds **1**–**3**.

	(1)	(2)	(3)
Empirical formula	$C_8H_{12}Cl_4N_4Zn$	$C_8H_{14}Br_2CdN_4O$	$C_8H_{12}Br_2CdN_4$
Formula weight	371.39	454.45	436.44
Temperature/K	293(2)	293(2)	293(2)
Crystal system	Monoclinic	Orthorhombic	Monoclinic
Space group	P2₁/n	Pnma	P2₁/c
Unit cell dimensions	$a = 7.9889(4)$Å	$a = 14.3391(8)$Å	$a = 4.0832(3)$Å
	$b = 12.6198(7)$Å	$b = 13.3491(10)$Å	$b = 14.7152(10)$Å
	$c = 12.9112(6)$Å	$c = 7.3241(5)$Å	$c = 10.2672(8)$Å
	$\beta = 101.333(5)°$	–	$\beta = 93.293(7)°$
Volume/Å³	1276.30(11)	1401.94(16)	615.89(8)
Z	4	4	2
ρ calc./mg mm⁻³	1.933	2.153	2.353
μ/mm⁻¹	2.742	7.245	0.235
$F(000)$	744	864	412
Crystal size/mm³	0.33 × 0.25 x 0.09	0.47 × 0.37 x 0.13	0.33 × 0.25 x 0.09
Theta range for data collection	3.21–29.00°	3.05–28.78°	3.98–29.37°
Index ranges	−9 ≤ h ≤ 10,	−16 ≤ h ≤ 19,	−5 ≤ h ≤ 5,
	−11 ≤ k ≤ 15	−13 ≤ k ≤ 17	−16 ≤ k ≤ 18
	−17 ≤ l ≤ 16	−9 ≤ l ≤ 8	−8 ≤ l ≤ 13
Reflections collected	6538	5252	2925
Independent reflections	2815 [$R(int)$ = 0.029]	1648 [$R(int)$ = 0.038]	1427 [$R(int)$ = 0.029]
Data/restraints/parameters	2815/0/173	1648/3/84	1427/0/83
Goodness-of-fit on F^2	1.035	1.007	1.038
Final R indexes [$I > 2\sigma (I)$]	$R1 = 0.0343, wR2 = 0.708$	$R1 = 0.0336, wR2 = 0.0709$	$R1 = 0.0308, wR2 = 0.0590$
Largest diff. peak/hole/e Å⁻³	0.246/−0.408	0.789/−0.727	0.637/−0.786

spectrum at 3434 and 3387 cm^{-1} are assigned to the asymmetric and symmetric stretching modes of water molecules. Structural X-ray diffraction data show the presence of the water molecule in the solid state of the complex (See below). The band located at 1621 cm^{-1} is assigned to the δ(H$_2$O) bending mode. Table S1 shows IR and Raman mode frequencies of 2-methylimidazole and its Cd(II) complex along with their corresponding assignment. As can be appreciate from Table S1, the observed band located at 3150 cm^{-1} in the IR spectrum of compound **2** (3148 cm^{-1} in Raman) can be assigned to the imidazole ring C—H stretching mode. The IR bands located at 2964 and 2927 cm^{-1} (2962 and 2924 cm^{-1} in Raman) are assigned to the CH$_3$ asymmetric and symmetric stretching modes, respectively. The 1700-1200 cm^{-1} frequency range is mainly characteristic for asymmetric and symmetric, C=C and C=N stretching modes of the imidazole ring as well as various C—H bending modes. When the aromatic ring nitrogen is involved in the complex formation, certain ring modes, particularly the ones in the 1600-1400 cm^{-1} spectral region, show a frequency blue-shifts both due to the coupling with M-N(ligand) bond vibrations and to the alterations of the ring force field [54,55]. The Raman bands located at 221 and 166 are assigned to the ν(Cd—Br) and ν(Cd—N) vibrations, respectively. These assignments are in accordance with corresponding reports in the literature [56].

In compounds **1** and **3**, the absence of water stretching ν(O—H) and bending δ(H$_2$O) bands indicates the formation of an anhydrous solid, which in turn suggests that it is deprived of metal centers with unsaturated coordination sites prone to attach water molecules. For both complexes, the most important bands related to vibrations of 1-methylimidazole are located between 1700 and 370 cm^{-1} showing small but detectable frequency shifts and intensity changes relative to the free ligand, which could reveal the molecule coordination to the metal center. The most pronounced changes are observed for the ν(C—N), ν(C—C), ν(ring) and δ(ring) modes, clearly denoting the extensive delocalization of the negative charge over the ring group. The Raman bands at 249 and 219 cm^{-1} are assigned to ν(Zn—Br) and ν(Cd—Br) modes, respectively [56]. The Raman bands observed at 158 and 155 cm^{-1} have been assigned to ν(Cd—N) and ν(Zn—N) stretching vibrations, respectively [56].

3.2. Thermal analysis

In order to characterize the compounds in terms of thermal stability, the thermal behavior of complexes **1**–**3** was examined by TG and DT analysis. The experiments were performed on samples consisting of numerous single crystals at ambient conditions with a heating rate of 5°/min (Fig. S5-S7).

The framework structure of compound **1** decomposes between 200 and 528 °C. However, it is difficult to determine the weight loss accurately in each stage because they are not resolved. The total mass loss at 528 °C observed experimentally was 83.24%, in accordance with the theoretical value (82.39%) considering that the final product was zinc metallic. The mass loss observed between 528 and 646 °C could be attributed to the volatilization of zinc metallic. The DTA curve of **1** shows an endothermic peak located at 202 °C without mass loss in TG, indicating the melting point of the substance. Three exothermic peaks are observed at 391, 428 and 469 °C, indicating the complex decomposition mechanism of this compound.

For complex **2**, the mass reduction corresponding to the loss of the water molecule occurs in the 64-110 °C thermal range, with an experimental mass loss of 3.69% (theoretical value: 3.96%). The dehydration process was observed at low temperature because the water molecule is weakly bonded, as showed by the crystal structure (See section 3.4.2). The second mass loss of 30.98% (theoretical

value: 36.04%) in the temperature range from 175 to 365 °C can be assigned to the release of two 2-methylimidazole ligands to form CdBr$_2$. The removal of bromide ligands and the volatilization of CdBr$_2$ occur in the 430−600 °C temperature range. The total mass loss observed experimentally at 600 °C was 97.90%. This behavior can be explained taking into account that CdBr$_2$ melts at 568 °C and then this compound volatilizes. The DTA curve of **2** shows an endothermic peak located at 74 °C indicating the release of the weakly bonded water molecule. The second endothermic peak at 143 °C (without mass loss in TGA) is assigned to the melting point of the sample. The third endothermic peak located at 291 °C in the DTA curve is associated to the removal of 2-methylimidazole ligands, in accordance with TGA data. The last two endothermic peaks at 471 and 514 °C are attributed to the decomposition of CdBr$_2$ followed by its volatilization.

The thermal decomposition of compound **3** is quite different and it decomposes in three steps. The first and the second steps are attributed to the removal of one 1-methylimidazole ligand with an experimental mass loss of 23.36% (theoretical value: 22.5%). The DTA curve shows two endothermic peaks located at 173 and 236 °C. The third step is completed at 320 °C with a mass loss of 13.32% and it is assigned to the removal of one imidazole ligand (theoretical mass loss: 15.12%). After that, the removal of bromide ligands and the volatilization of CdBr$_2$ occur in the range from 450 to 600 °C, similar to compound **2**.

3.3. Fluorescence properties

Taking into account the excellent luminescent properties of coordination compounds with d^{10} metal centers, solid state luminescent studies of the three complexes **1**−**3** were performed. Fig. 1 shows the fluorescence spectra of compounds **1**, **2** and **3** obtained with an excitation λ$_{ex}$ of 370 nm. The free organic ligand (2-methylimidazole) shows a stong fluorescence centered at 480 nm (λ$_{ex}$ = 380 nm) and it was assigned to π→π* transitions [57]. Since the Cd(II) and Zn(II) ions are difficult to oxidize or reduce because of the relatively inert d^{10} configuration, the nature of the emission by these compounds is neither metal-to-ligand charge transfer (MLCT) nor ligand-to-metal charge transfer (LMCT). Up on excitation at 370 nm, the Zn complex exhibits an emission bands at 440 and 530 nn. The emission bands at higher energy could be attributed to intra-ligand (π→π*) transitions, while the low-energy band
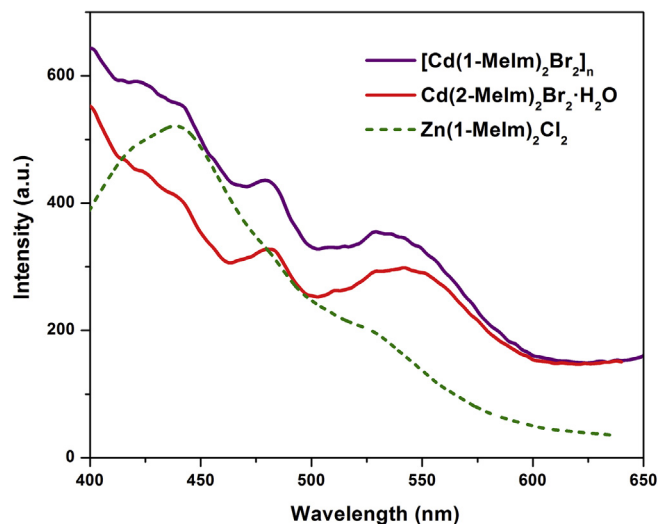

Fig. 1. Solid-state fluorescence spectra of compounds **1**, **2** and **3** at room temperature.

probably originates from LMCT [58]. The shoulder located at 480 nm is assigned to $\pi \rightarrow \pi^*$ transitions corresponding to the ligand. Compounds **2** and **3** exhibit unsymmetrical emission as a pair of bands at 440 and 442 nm and correspondingly at 482 and 480, respectively, due to intra-ligand and LMCT transitions as in compound **1**. The emission bands located at 543 nm in both complexes are also due to LMCT. For complexes **2** and **3**, the luminescence intensity gradually decreases with the presence of crystallization water molecules. The weak fluorescence emission from compound **2** may be attributed to the vibrational quenching of water molecules [59].

3.4. Description of crystal structures

3.4.1. Crystal structure of [ZnL₂Cl₂], L = 1-methylimidazole (1)

Fig. 2 shows an ORTEP drawing of the complex and bond distances and angles around the metal are included in Table 2. The Zn(II) complex appears as mono-nuclear units in the crystal, weakly bonded to one another through C−H⋯Cl and van der Waals interactions. The Zn(II) ion is at a general crystal position in a tetrahedral environment, coordinated to two chloride ions [Zn−Cl bond distances of 2.2429(7) and 2.2400(8)Å, ∠(Cl−Zn−Cl) = 118.15(3)°] and to two pyridine-like N-atom of two 1-methylimidazole ligands [Zn−N bond distances of 2.011(2) and 2.007(2) Å, ∠(N−Zn−N) = 108.75(9)°]. The Cl−Zn−N bond angles are in the range 103.94(6)-111.45(7)°. The molecular crystal is further stabilized by weak van der Waals and C−H⋯Cl bonds [C⋯Cl bond lengths from 3.508 to 3.888 Å and C−H⋯Cl angles in the 129.7−159.4° range].

In the crystal packing of compound **1**, the molecules are linked via non-classical C−H⋯Cl hydrogen bonds generating $R_2^2(14)$, $R_4^2(20)$ and $R_4^3(19)$ graph-set ring motifs (Fig. 3, Table 3). The supramolecular architecture of this complex also includes the existence of intermolecular C−H⋯π and Zn−Cl⋯π interactions (Fig. 4) as described in Table 4.

3.4.2. Crystal structure of [CdL'₂Br₂]·H₂O, L' = 2-methylimidazole (2)

The Cd(II) complex appears in the solid as distinct units, linked through H-bonds mediated by a crystallization water molecule. Fig. 5 shows an ORTEP drawing of the substance. Bond distances and angles around the metal are included in Table 2. The Cd(II) ion lies on a crystallographic mirror plane in a tetrahedral environment, coordinated to two on-plane bromide ions [Cd−Br bond distances of 2.5767(8) and 2.5940(7) Å, ∠(Br−Cd−Br) = 109.12(3)°] and to the pyridine-like N-atom of two mirror-related 2-methylimidazole ligands [d(Cd−N) = 2.209(3)Å, ∠(N−Cd−N) = 118.23(16)°]. The Br−Cd−N bond angles are 106.76(8) and 107.86(8)°. A crystallization water molecule, also onto a crystal mirror plane, acts as acceptor in a Ow⋯H−N (imdz)

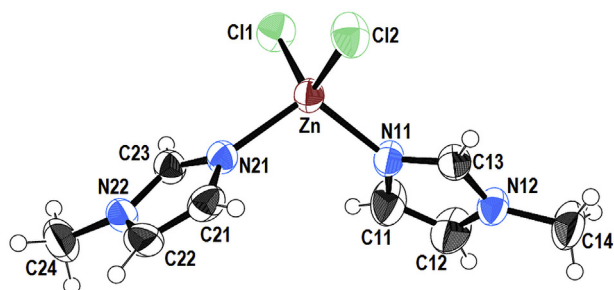bond [d(N⋯Ow) = 2.908 Å, ∠(N−H⋯Ow) = 159.4°] bridging molecules along the crystal b-axis. In addition, the water molecule acts as donor in two Ow-H⋯Br bonds linking molecules along the c-axis [Ow⋯Br distances of 3.381 and 3.416 Å; Ow-H⋯Br angles of 172.6 and 174.8°]. These interactions give rise to a H-bonded layered structure perpendicular to the a-axis.

In the case of complex **2**, molecules are linked via C−H⋯Br hydrogen bonds forming $R_2^1(8)$ rings, and also interconnected by water molecules via O−H⋯N hydrogen bonds to form $R_7^4(24)$ motifs (Fig. 6). The structure of **2** is also stabilized by intermolecular π⋯π interactions with off set facial arrangement [60] as described in Table 5.

3.4.3. Crystal structure of [CdL₂Br₂]ₙ, L = 1-methylimidazole (3)

Fig. 7 shows an ORTEP drawing of the polymer and bond distances and angles around the metal are included in Table 2. The Cd(II) ion is sited on a crystallographic inversion centre in a squashed octahedral environment, CdBr₄L₂, equatorially coordinated to four symmetry related bromide anions [Cd−Br bonds distances of 2.8204(4) and 2.8710(5) Å] and axially to the pyridine-like N-atoms of two inversion-related 1-methylimidazole ligands [d(Cd−N) = 2.277(3) Å]. Adjacent, equatorially edge-sharing, octahedra are related to each other through another inversion centre, hence giving rise to a polymeric structure that extends along the crystal a-axis where neighboring Cd(II) ions are bridged by a pair of bromide ions and are apart from each other in the unit cell length a [= 4.0832(3) Å]. Acute trans Br−Cd−Br angles is 88.32(1)° and the axial Cd−N bond is at right angle with the equatorial plane to within experimental accuracy. The structure is stabilized by weak intra- and inter-chain C−H⋯Br interactions [C⋯Br distances from 3.609 to 4.000 Å and C−H⋯Br angles from 118.7 to 162.2°].

Packing of structure **3** shows a pattern of C−H⋯Br hydrogen bonds forming $R_4^4(26)$ and $R_4^4(27)$ synthons (see Fig. 8a), as well as π⋯π interactions with offset facial arrangement (Fig. 8b) as described in Table 5 [60].

3.5. Hirshfeld surface analysis

For a complete understanding of the combined participation of hydrogen bonds and π-stacking interactions in the context of supramolecular self-assembly of title compounds, the Hirshfeld surfaces [61−64] and the associated 2D fingerprint plots were calculated. The Hirshfeld surface in a crystal enables identification of the regions of particular importance to intermolecular interactions. Fig. 9 shows surfaces mapped over the d_{norm} for compounds **1**−**3**. The red regions labeled 1 in the d_{norm} map for compound **1** are attributed to C−H⋯Cl hydrogen bonds, while a pale blue to white spot (labeled 2) represents C⋯H contacts associated to weak C−H⋯C hydrogen bonds. The contacts associated to chlorine atom represent the strongest intermolecular hydrogen bond interaction in the crystal of **1**, as reflected by the geometrical parameters showed in Table 3. In compound **2**, the Br⋯H contacts can be seen as two large and bright red areas along with light red spots (labeled 3) representing C−H⋯Br hydrogen bonds. This indicates different ways of Br⋯H contacts in different regions of the molecule. Other bright red spot (labeled 4) corresponds to the strongest N−H⋯O hydrogen bond indicating contacts of the water molecule as depicted in Fig. 6. White visible spots labeled 2 on the surface are due to weak C−H⋯C hydrogen bonds. In addition to these hydrogen bonds, C⋯C contacts are clearly visible as a pair of white spots in agreement to results showed in Fig. 6. In structure **3**, the small extent of area and light red spots labeled 3 indicate C−H⋯Br hydrogen bonds as in structure **2**, while two dominant large and bright regions (labeled 6) are attributed a short Cd⋯Br

Fig. 2. Molecular structure of compound **1**. Displacement ellipsoids are drown at the 50% probability level.

Table 2
Selected bond lengths and angles for compounds **1**–**3** (Å,°).

ZnL$_2$Cl$_2$ (1)		[CdL′$_2$Br$_2$]·H$_2$O (2)		[CdL$_2$Br$_2$]$_n$ (3)	
Zn–N(11)	2.011(2)	Cd–N(1)	2.209(3)	Cd–N(1)	2.277(3)
Zn–N(21)	2.007(2)	Br(1)–Cd	2.5767(8)	Cd–Br	2.8204(4)
Zn–Cl(1)	2.2429(7)	Br(2)–Cd	2.5940(7)	Cd–Br#3	2.8710(5)
Zn–Cl(2)	2.2400(8)				
N(21)–Zn–N(11)	108.75(9)	N(1)–Cd–N(1)#4	118.2(2)	N(1)–Cd–Br	90.01(8)
N(21)–Zn–Cl(2)	111.45(7)	N(1)–Cd–Br(1)	107.86(8)	N(1)–Cd–Br#1	89.99(8)
N(11)–Zn–Cl(2)	106.27(7)	N(1)–Cd–Br(2)	106.76(8)	N(1)–Cd–Br#2	89.48(8)
N(21)–Zn–Cl(1)	103.94(6)	Br(1)–Cd–Br(2)	109.12(3)	Br–Cd–Br#2	91.68(1)
N(11)–Zn–Cl(1)	108.01(7)			N(1)–Cd–Br#3	90.52(8)
Cl(2)–Zn–Cl(1)	118.15(3)			Br–Cd–Br#3	88.32(1)
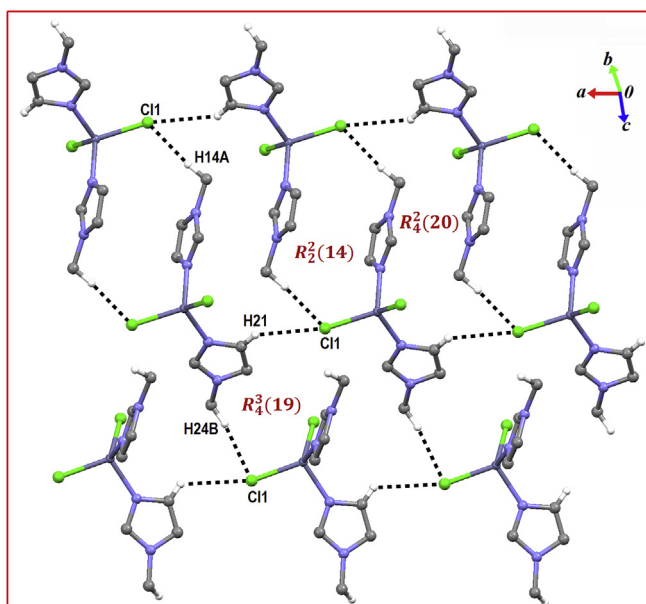
Fig. 3. A view of the hydrogen-bonding interactions for compound **1** (dashed lines).
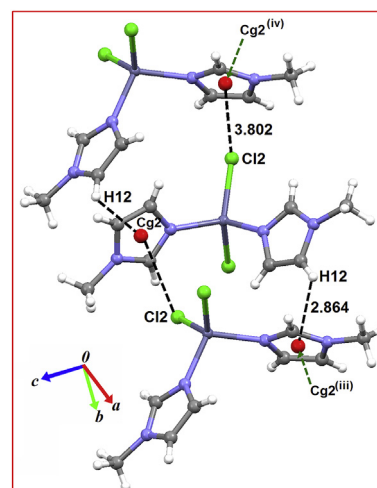
Fig. 4. A view of the π-stacking interactions for compound **1** showing H···Cg2 and Cl···Cg2 contacts (dashed lines). *Symmetry codes*: (iii) 3/2-x, -½+y, ½-z; (iv) 3/2-x, ½+y, ½-z.

Table 3
Hydrogen bond interactions for compounds **1**–**3**(Å,°).

D—H···A	d(D—H)	d(H···A)	d(D···A)	∠(D—H···A)	Label (Fig. 3)
Compound **1**					
C14–H14A···Cl1[i]	0.97(4)	2.83(4)	3.710(5)	152	1
C21–H21···Cl1[ii]	0.85(3)	2.92(3)	3.510(3)	128	–
C24–H24B···Cl1[iii]	0.961(4)	2.877(1)	3.797(4)	161	–
C12–H12···C22[iv]	0.95(5)	2.97(5)	3.764(5)	142	2
Compound **2**					
C1–H1···Br1[i]	0.930(4)	3.023(1)	3.876(4)	153	–
O1W–H1W···Br2[ii]	0.86(2)	2.53(3)	3.381(6)	173	3
O1W–H2W···Br1[iii]	0.86(1)	2.56(1)	3.416(4)	175	3
N2–H2A···O1W	0.860(3)	2.087(3)	2.908(3)	159	4
C4–H4C···C3[iii]	0.960(4)	3.096(4)	3.395(6)	100	2
Compound **3**					
C2–H2···Br[i]	0.91(4)	3.05(4)	3.924(5)	162	3
C1–H1···Br[ii]	0.88(4)	2.96(4)	3.610(4)	133	3
C3–H3···Br	0.93(5)	2.89(6)	3.538(5)	127	–
C4–H4C···Br[iii]	0.960(6)	3.126(1)	3.684(6)	119	–
C4–H4B···Br[iv]	0.960(5)	3.115(1)	4.000(6)	154	–

Symmetry codes for (**1**): (i) 1-x, 1-y, 1-z; (ii) −1+x, y,z; (iii) -½+x, -½-y, ½+z; (iv) ½-x, ½+y, 1.5-z; for (**2**):(i) -½+x, 1.5-y, -½-z; (ii) 1.5-x, 1-y, -½+z (iii) 1.5-x, 1-y, ½+z; for (**3**): (i) x+1, -y+½, z-½; (ii) 1-x, -½+y, 1.5-z; (iii) -x, y-½, -z+3/2; (iv) x, -y + x, -y+½, z-½, z-x, -y+½, z-½.

contacts. C···C contacts are visible as two small red regions labeled 5, in accordance to Fig. 8.

In order to explorer the presence of C···C interplanar contacts in compounds **2** and **3**, a close examination with *Shape index* and *Curvedness* - Hirshfeld surface properties generally used to identify planar stacking arrangements - was performed [33]. The pattern of

Table 4
Geometrical parameters of C—H⋯π* and Y-X⋯π**interactions for compound **1** (Å,°).

C—H⋯Cg(j)[a]	H⋯Cg	H-perp[b]	γ[c]	∠C—H⋯Cg(j)	H⋯C[d]
C12—H12⋯Cg(2)[i]	2.86	2.85	6.37	139	3.633(1)
-X(i)⋯Cg(j)[a]	X⋯Cg	X-perp[b]	γ[c]	∠Y-X⋯Cg(j)	
Zn—Cl2⋯Cg(2)[ii]	3.802(1)	3.514	22.43	147	—

Symmetry codes: (i) 3/2-x, −½+y, ½-z, (ii) 3/2-x, ½+y, ½-z.*(H⋯Cg < 3.0 Å, γ < 30.0°). ** (X⋯Cg < 4.0 Å, γ < 30.0°).
[a] Centroid of C1−C4/C8−C9 ring.
[b] Perpendicular distance of H to ring plane J.
[c] Angle between the Cg-H vector and ring J normal.
[d] Distance between H-atom and the nearest carbon atom in the aromatic ring.

Table 5
Geometrical parameters for the π-stacking moieties involved in the π⋯π interactions for compounds **2** and **3**(Å,°).

Rings i-j[a]	Rc[b]	R1v[c]	R2v[d]	α[e]	β[f]	γ[g]	Slippage[h]
Compound **2**							
Cg(1)⋯Cg(1)[i]	3.5508(3)	3.395(1)	3.395(1)	0.00	17.1	17.1	1.042
Compound **3**							
Cg(3)⋯Cg(3)[ii]	4.0832(3)	3.350(1)	3.350(1)	0.00	34.9	34.9	2.334

Symmetry codes: (i) 1-x, -y, 1-z, (ii) 1 + x, y, z.
[a] Cg(1) and Cg(3) are the centroids of N1−N2/C1−C3 ring.
[b] Centroid distance between ring i and ring j.
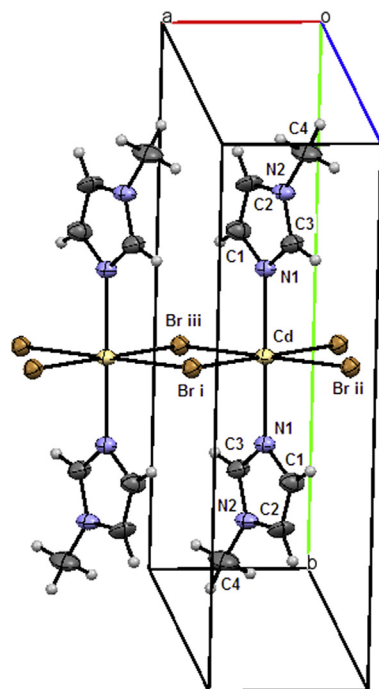[c] Vertical distance from ring centroid i to ring j.
[d] Vertical distance from ring centroid j to ring i.
[e] Dihedral angle between mean planes i and j.
[f] Angle between the centroid vector Cg(i)⋯Cg(j) and the normal to the plane (i).
[g] Angle between the centroid vector Cg(i)⋯Cg(j) and the normal to the plane (j).
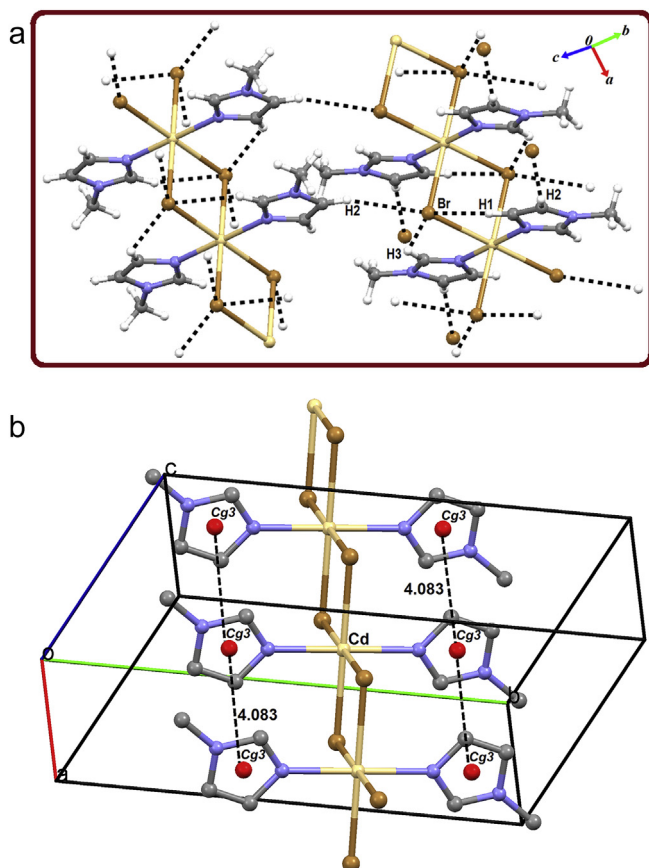[h] Distance between Cg(i) and normal projection of Cg(j) on ring i.

Fig. 5. Molecular structure of compound **2**. Displacement ellipsoids are drawn at the 50% probability level.
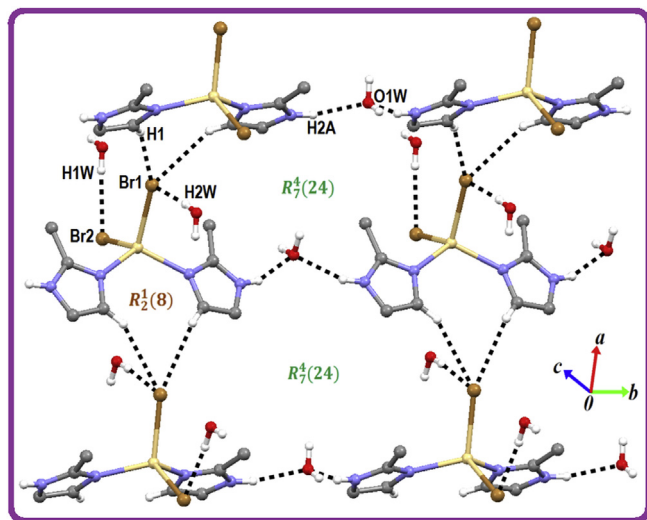
Fig. 6. A view of the hydrogen-bonding interactions (dashed lines) for compound **2**.

Fig. 7. View of poly-nuclear [CdL₂Br₂]ₙ complex down the crystal *c*-axis, showing the labeling of the atoms and their displacement ellipsoids at the 50% probability level. Crystal symmetry operations: (i) 1-x, 1-y, 1-z; (ii) −x, 1-y, 1-z; (iii) 1 + x, y, z.

touching red and blue triangles on the *shape index* surfaces (highlighted circles in Fig. 10) is characteristic of π-π stacking of five-membered rings [35]. However, the pattern of triangles is more prominent in structure **2** that in structure **3**, consisting with the geometrical descriptors reported in Table 5. The existence of π-π interactions for compounds **2** and **3** is also evident as relatively large and green flat regions delineated by blue circles on the corresponding *Curvedness* surfaces (Fig. 10, column 2) [33].

Fingerprint plots [65,66] for the main intermolecular contacts of compounds **1**−**3** are shown in Fig. 11. The sizes and shapes of the fingerprint illustrate the significant differences between the intermolecular interaction patterns. The fingerprint plots can be decomposed to highlight particular atoms pair close contacts,

allowing separation of contributions from different interaction types, which generally overlap in the full fingerprint.

H⋯H intermolecular interactions (labeled 1) are the shortest and most abundant contacts for the three compounds. These contacts are not visible on the corresponding Hirshfeld surfaces because their distances are significantly longer than the sum of the van der Waals radii. In structure **1**, the pair of narrow pointed spikes labeled 2 and 3 around ($d_e + d_i$) of 2.8 and 3.0 Å show the presence of Cl⋯H and C⋯H contacts, respectively. In addition, the decomposed fingerprint plot shows C—H⋯C hydrogen bonds of which C—H⋯π interactions (column 2) appear as a pair of characteristic "wings" [35] around ($d_e + d_i$) = 2.8 Å. In structure **2**, the H⋯H contact fingerprint is very broad indicating the existence of a large range of intermolecular distances ($d_e + d_i$) for this interaction.

Furthermore, the structure is dominated by a single sharp spike (labeled 6) at ($d_e + d_i$) around 2.0 Å, due to shortest O⋯H contacts revealing the occurrence of C—H⋯O hydrogen bonds. Even more, a pair of sharp and asymmetric spikes labeled 4 represents Br⋯H

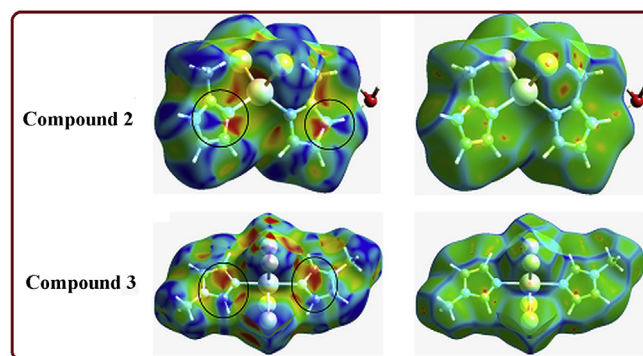**Fig. 10.** Hirshfeld surfaces mapped with *shape index* and *curvedness* for compounds **2** and **3**.

Fig. 8. A view of (a): hydrogen-bonding interactions (dashed lines) and (b): π-stacking interactions (with intercentroid distance) for compound **3**.
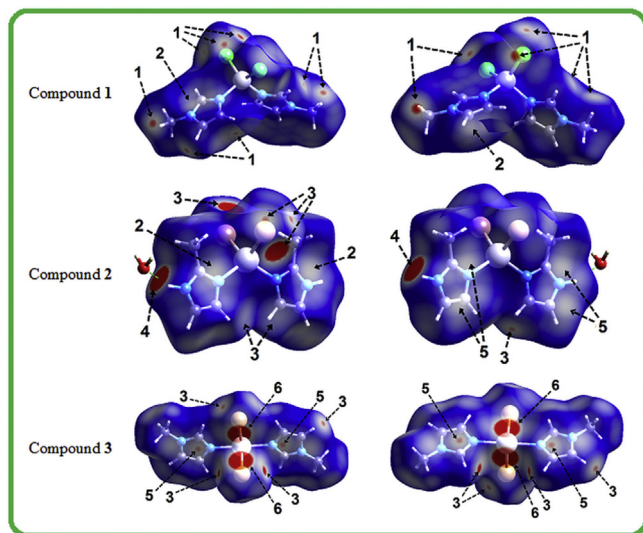
Fig. 9. Hirshfeld surfaces mapped with d_{norm} for molecules **1—3** in two orientations: molecule in column 3 rotated by 180° around the horizontal axis of the plot; Thermal ellipsoids at 50% probability level; numbered arrows are discussed in the text.

contacts associated to O—H···Br hydrogen bonds. The spike at the top left ($d_i < d_e$) corresponds to points on the surface around the O—H donor, whereas that at the bottom right ($d_e > d_i$) corresponds to Br acceptor inside the surface. A distinctive fingerprint on the diagonal of the plot for structure **2** at around $d_e = d_i \approx 1.8$ Å is due

to C···C contacts labeled 7 (Fig. 11, column 2), which are identified as result of π···π interactions [33].

In the case of structure **3**, the fingerprint of H···H contacts (labeled 1) differs from the same region on the fingerprint found in structure **2**, indicating intermolecular distances near to 2.4 Å. In comparison with structure **2**, we observe a pair of less sharp and symmetric spikes (labeled 4) representing Br···H contacts associated to O—H···Br hydrogen bonds. Like structure **2**, C···C contacts (labeled 7) are present in structure **3** revealing π···π stacking interactions, which are identified as a region of pale blue to green colour (column 2) on the diagonal at around $d_e = d_i \approx 1.8$ Å [33].

Unlike the mono-nuclear Cd(II) complex, we have found an interesting fingerprint plot corresponding to Br···Cd intermolecular contacts (column 3) for the poly-nuclear Cd(II) complex. Other minor contacts such as Cl···C and C···N for structures **1** and **2**, respectively, are also visible (Fig. 11, column 3), emphasizing the observed differences between the intermolecular interactions patterns.

The relative contributions of the main intermolecular contacts in title compounds are shown as histogram in Fig. 12. For all the compounds, H···H contacts have a major contribution to the Hirshfeld surface, varying from 37% in compound **2**—44% in compound **3**. The proportions of C···H and N···H contacts are similar in the three compounds comprising 10—11 and 7—9% of total Hirshfeld surface area, respectively. The N···H contacts are associated to C—H···N hydrogen bonds, which are not visible in the Hirshfeld surfaces due to the H···N distances are significantly longer than sum of the van der Waals radii for all three complexes.

The high percentage of 34% for Cl···H contacts in structure **1**, and 26—32% for Br···H contacts in structures **2** and **3**, are relevant contributions to crystal packing in these compounds. In addition, the Br···Cd contacts account for 7.5% of total Hirshfeld surface area in compound **3**, which is a comparable contribution to those of C···H and N···H contacts previously reported. By the other hand, an evident contribution of 2% from π···π contacts for the two Cd(II) complexes is a distinctive feature related to the Zn(II) complex. Finally, Cl···C and C···N contacts with minor value of 1.6%, also contribute to the crystal stability of structures **1** and **2**, respectively.

3.6. Molecular electrostatic potential analysis

To get a better understanding towards the attractive character of weak intermolecular hydrogen bonds for packing stabilization, we have computed the molecular electrostatic potentials (ESP) mapped on electron density isosurface of complexes **1—3** (Fig. 13), highlighting the blue and red colors for positive and negative regions, respectively. The existence of a direct relationship between
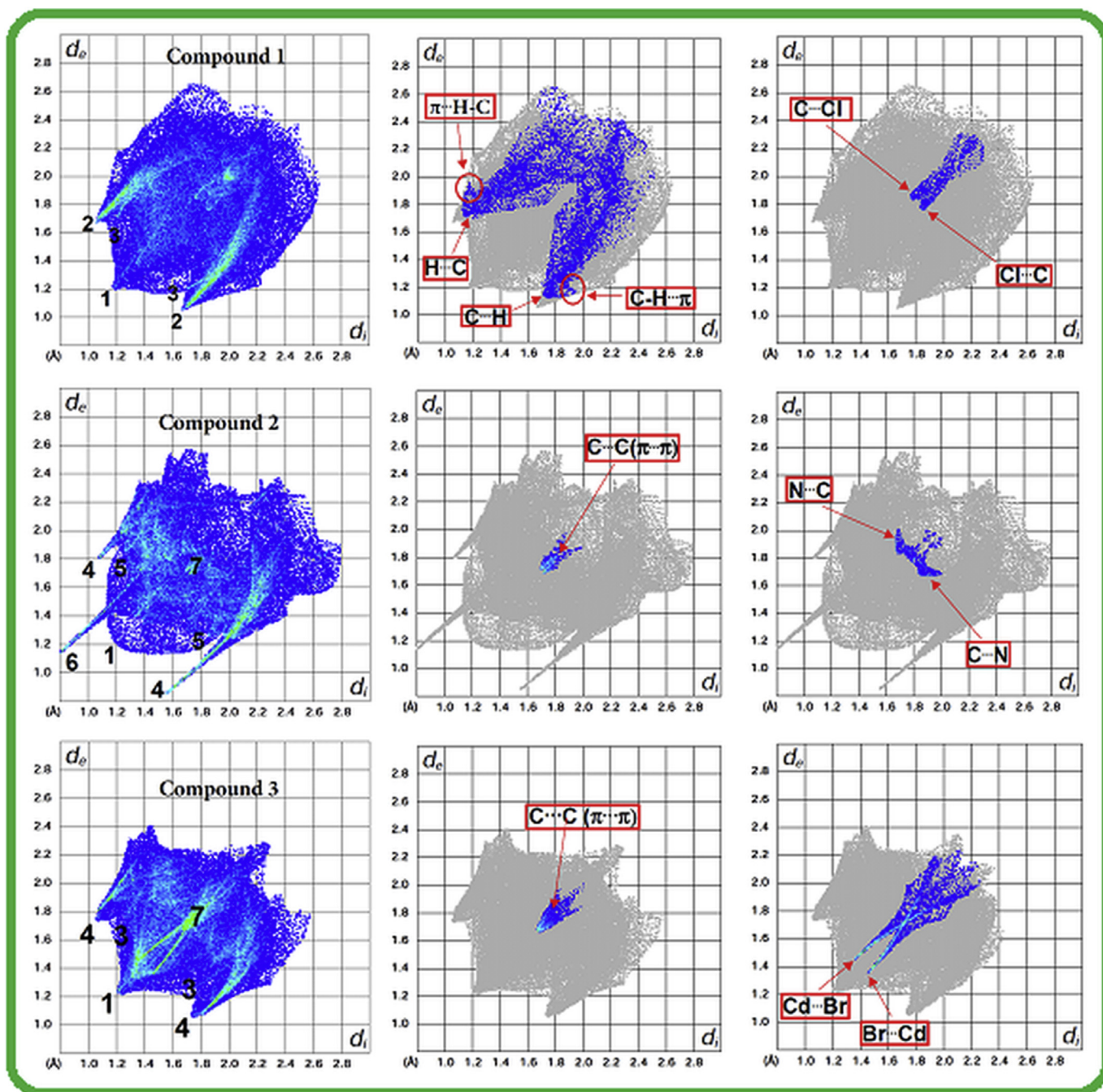
Fig. 11. Fingerprint plots for compounds **1**–**3** showing (1) H···H, (2) Cl···H, (3) C···H, (4) Br···H, (5) N···H, (6) O···H and (7) C···C intermolecular contacts.
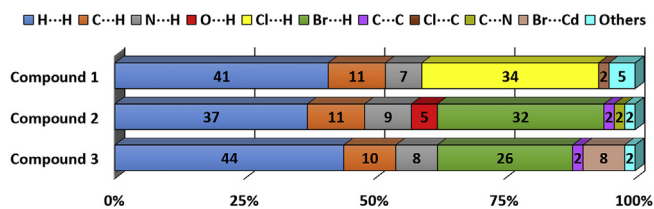

Fig. 12. Relative contributions to the Hirshfeld surface area for the main intermolecular contacts in the complexes **1**–**3**.

ESP and molecular dipole moment (μ) [67,68], prompted us to

calculate the experimental dipole moments of the molecules for the three structures by using MOPAC (Molecular Orbital PACkage) [69] program with PM7 semi-empirical method.

Molecular ESP for complex **1** (Fig. 13a) reveals a highly polar molecule ($\mu = 9.56$ D) with a deep red region of highly negative electrostatic potential (-0.102 au) surrounding the two chlorine atoms, and three complementary deep blue regions with highest positive electrostatic potential values of 0.092, 0.075 and 0.068 au in the vicinity of H14A, H24B and H21 hydrogen atoms, respectively. These results help to explain the formation and strength of C−H···Cl hydrogen bonds in this structure, due to the variation of electropositive values occurs in the same order observed for H−Cl bond distances (Table 3).
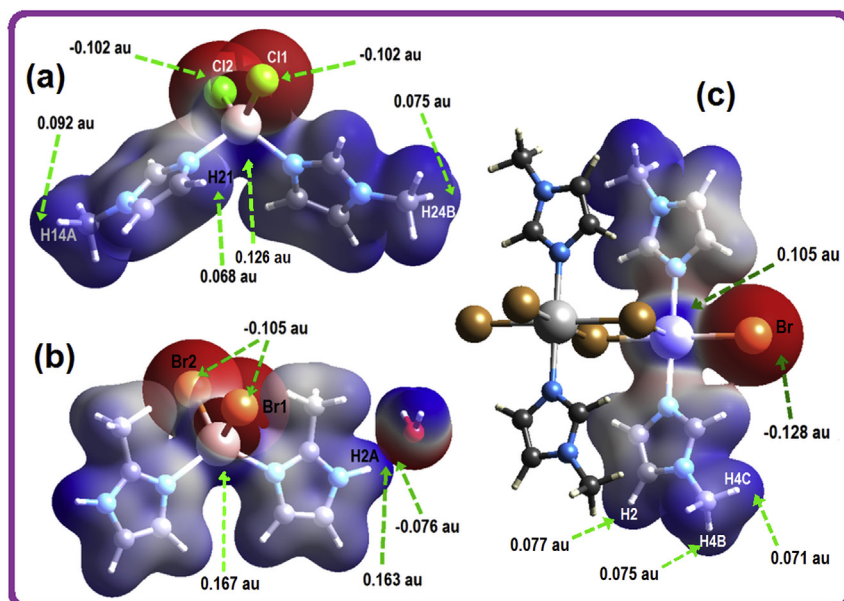
Fig. 13. Electron density surfaces mapped with electrostatic potential (ESP) over the range ± 0.170 au for compounds **1**—**3**. The isosurfaces are drawn at 0.008 eau^{-3}.

Like in complex **1**, the molecular ESP surface for complexes **2** and **3** displays high polarity with dipole moments of 8.02 and 9.05 D, respectively, and similar electrostatic complementarity showing deep red regions of high electronegative potentials (−0.105 au for **2** and -0.128 au for **3**) around the bromine atoms. However, on the complex **2** surface (Fig. 13b), the ESP reaches the highest electropositive value of 0.163 au near the H2A atom attached to strong N2 donor, and a strong electronegative region (−0.076 au) is found around the O1W- atom on the surface of a neighbor water molecule. This favours the formation of strongest N−H···O hydrogen bond as described in Table 3. On the complex **3** surface (Fig. 13c), three similar ESP electropositive values ranging from 0.071 to 0077 au around H4, H4B and H2 atoms indicate similar strength of the corresponding intermolecular C−H···Br hydrogen bonds in this structure, in agreement with the geometry reported in Table 3. It is interesting to highlight highest electropositive values nearby to the metal ion for the three structures, which explain the electrostatic nature of Zn−Cl bonds for complex **1**, and Cd−Br for complexes **2** and **3**.

4. Conclusions

A novel mono-nuclear Zn(II)-chloro complex and two Cd(II)-bromo complexes (one mono- and the other poly-nuclear) based on methylimidazole as ligand have been prepared and characterized by spectroscopic and thermal studies. The solid state fluorescence properties of those three complexes were investigared and it has been assumed that the observed luminescence was a consequence of intraligand ($\pi \rightarrow \pi^*$) transitions. The fluorescence intensity in the Cd(II) complexes is observed to be controlled by the presence of crystallization water molecules that produce a vibrational quenching decreasing the emission bands intensities. The fluorescence properties of the compounds imply that they may be good candidates for optical materials. The crystal structures of the compounds were determined by X-ray diffraction methods and different packing motifs combining hydrogen bonds and π-stacking interactions were identified. Hirshfeld surface analysis and breakdown of the corresponding 2D-fingerprint plots provides a convenient way of quantifying intermolecular interactions within the crystal structures. The fingerprint plots enabled us to decode the intermolecular interaction types present in the title structures, revealing that H···H contacts comprise the majority of interactions, and identifying C−H···π contacts for the Zn(II) complex. The d_{norm} surfaces showed dominant X···H (X = Cl, Br) contacts for all the three compounds, whereas *Shape index* and *Curvedness* were useful to visualize and analyze π-π stacking in compounds **2** and **3**. These results underline the utility of the Hirshfeld surfaces as important methodology in the modern crystal engineering for the design of crystalline Zn(II)-halo and Cd(II)-halo complexes with imidazole derivatives as ligands. Molecular electrostatic potential maps allowed a visual and quantitative study on the strength and electrostatic nature of weak intermolecular hydrogen bonds in the crystal stabilization of the three complexes. These results can be useful for the prediction of supramolecular motifs in this type of coordination compounds.

Appendix A. Supplementary data

Supplementary data related to this article can be found at http://dx.doi.org/10.1016/j.molstruc.2017.01.028.

References

[1] J. Saju, M. Ahmad, P.K. Bharadwaj, Structural diversity and luminescence properties of coordination polymers built with a rigid linear dicarboxylate and Zn(II)/Pb(II) ion, Cryst. Growth Des. 13 (2013) 2618.
[2] F.F. Yang, X.F. Wang, X.Y. Yu, Y.H. Luo, H. Zhang, Coordination polymers of the bis(imidazole) ligand modulated by dicarboxylate ligands: from 2D layer to 3D framework, Polyhedron 98 (2015) 40.
[3] Metal-Organic frameworks as sensors: a ZIF-8 based Fabry−Pérot device as a selective sensor for chemical vapors and gases, J. Am. Chem. Soc. 132 (2010) 7832.
[4] H. Tan, B. Liu, Y. Chen, Lanthanide coordination polymer nanoparticles for

sensing of mercury(II) by photoinduced electron transfer, ACS Nano 6 (2012) 10505.

[5] K. Ooi, Y. Tasaki-Handa, Y. Abe, A. Wakisawa, Lanthanide ion exchange properties of a coordination polymer consisting of di(2-ethylhexyl) phosphoric acid and trivalent metal ions (Ce^{3+}, Fe^{3+}, or Al^{3+}), Dalton Trans. 43 (2014) 4807.

[6] R.A. Agarwal, A. Aijaz, M. Ahmad, E.C. Sanudo, Q. Xu, P.K. Bharadwaj, Two new coordination polymers with Co(II) and Mn(II): selective gas adsorption and magnetic studies, cryst, Growth Des. 12 (2012) 2999.

[7] G. Zhuang, W. Chen, J. Zheng, H. Yu, J. Wang, N-(sulfoethyl) iminodiacetic acid-based lanthanide coordination polymers: synthesis, magnetism and quantum Monte Carlo studies, J. Solid State Chem. 192 (2012) 284.

[8] A. Santra, I. Senkovska, S. Kaskel, P.K. Bharadwaj, Gas storage in a partially fluorinated highly stable three-dimensional porous metal—organic framework, Inorg. Chem. 52 (2013) 7358.

[9] F.X. Bu, M. Hu, L. Xu, Q. Meng, G.Y. Mao, D.M. Jiang, J.S. Jiang, Coordination polymers for catalysis: enhancement of catalytic activity through hierarchical structuring, Chem. Commun. 50 (2014) 8543.

[10] X. Gu, Z.H. Lu, H.J. Jiang, T. Akita, Q. Xu, Synergistic catalysis of metal—organic framework-immobilized Au—Pd nanoparticles in dehydrogenation of formic acid for chemical hydrogen storage, J. Am. Chem. Soc. 133 (2011) 11822.

[11] F. Luo, Y.X. Che, J.M. Zheng, Trinuclear cobalt based porous coordination polymers showing unique topological and magnetic variety upon different dicarboxylate-like ligands, Cryst. Growth Des. 9 (2009) 1066.

[12] P. Kanoo, K.L. Gurunatha, T.K. Maji, Temperature-controlled synthesis of metal-organic coordination polymers: crystal structure, supramolecular isomerism, and porous property, Cryst. Growth Des. 9 (2009) 4147.

[13] H. Zhang, X. Wang, K. Zhang, B.K. Teo, Crystal engineering in [(12C4)₂Na] [Cd(SCN)₃]: first example of an anionic cadmium thiocyanate coordination solid with a sandwich $[(12C4)_2Na]^+$ cation as spacer/controller, resulting in a hexagonal arrangement of antiparallel zigzag $[Cd(SCN)_3]_\infty$ chains, Inorg. Chem. 37 (1998) 3490.

[14] H.J. Chen, X.M. Chen, Crystal structures of two- and three-dimensional polymeric complexes assembled by metal pseudohalides and 4-aminobenzoic acid via hydrogen bonds and covalent bonds, Inorg. Chim. Acta 329 (2002) 13.

[15] P. Chakraborty, A. Guha, S. Das, E. Zangrando, D. Das, Phenoxo bridged luminescent dinuclear zinc(II) and cadmium(II) complexes of 2-[[[2-(2-pyridyl)ethyl]imino]methyl]phenol: crystal structure, photophysical and thermal studies, Polyhedron 49 (2013) 12.

[16] G. Chalasinski, M.M. Szczesniak, State of the art and challenges of the ab initio theory of intermolecular interactions, Chem. Rev. 100 (2000) 4227.

[17] (a) G.R. Desiraju, Crystal engineering: from molecule to crystal, J. Am. Chem. Soc. 135 (2013) 9952—9967;
(b) G.R. Desiraju, A bond by any other name, Angew. Chem. Int. Ed. 50 (2011) 52—59;
(c) J.D. Dunitz, A. Gavezzotti, Supramolecular synthons: validation and ranking of intermolecular interaction energies, Crys Growth Des. 12 (2012) 5873—5877.

[18] E.A. Meyer, R.K. Castellano, F. Diederich, Interactions with aromatic rings in chemical and biological recognition, Angew. Chem. Int. 42 (2003) 1210.

[19] M. Ben Nasr, F. Lefebvre, C. Ben Nasr, Synthesis, crystal structure and infrared characterization of bis(4-dimethylamino-pyridinium) tetrachlorocuprate, Amer. J. Anal. Chem. 6 (2015) 446—456.

[20] D.N. Sredojević, Z.D. Tomićand, S.D. Zarić, Evidence of Chelate—Chelate stacking interactions in crystal structures of transition-metal complexes, Cryst. Growth Des. 10 (2010) 3901—3908.

[21] H. Suezawa, T. Yoshida, Y. Umezawa, S. Tsuboyamaand, M. Nishio, CH/π interactions implicated in the crystal structure of transition metal compounds — a database study, Eur. J. Inorg. Chem. 12 (2002) 3148—3155.

[22] D.A. Carter, J.E. Pemberton, Raman spectroscopy and vibrational assignments of 1- and 2-methylimidazole, J. Raman Spectrosc. 28 (1997) 939.

[23] C.M. Jones, C.R. Johnson, S.A. Asher, R.E. Shepherd, Resonance Raman studies of the excited electronic states of imidazolepentacyanoferrate(III)(2-) and imidazolepentaammineruthenium(III)(3+) ions, J. Am. Chem. Soc. 107 (1985) 3772.

[24] C.C. Su, J.H. Chen, K.Y. Hwang, S.L. Liu, S.W. Wang, S.L. Wang, S.N. Liu, Bonding properties of Cu(II)-imidazole chromophores: spectroscopic and electrochemical properties of monosubstituted imidazole copper(II) complexes. Molecular structure of [Cu(4-methylimidazole)₄(ClO₄)₂], Inorg. Chim. Acta 231 (1992) 196.

[25] R. Carballo, A. Castiñeiras, B. Covelo, E. García-Martínez, J. Niclós, E.M. Vázquez-López, Solid state coordination chemistry of mononuclear mixed-ligand complexes of Ni(II), Cu(II) and Zn(II) with α-hydroxycarboxylic acids and imidazole, Polyhedron 23 (2004) 1505.

[26] S. Abuskhuna, M. McCann, J. Briody, M. Devereux, V. McKee, Synthesis and structure of Mn(II), Cu(II) and Zn(II) complexes containing bis-imidazole ligands, Polyhedron 23 (2004) 1731.

[27] M.B. Bushuev, B.A. Selivanov, N.V. Pervukhina, D.Y. Naumov, M.I. Rakhmanova, L.A. Sheludyakova, A.Y. Tikhonov, S.V. Larinov, Luminescent zinc(II) and cadmium(II) complexes based on 2-(4,5-dimethyl-1H-imidazol-2-yl)pyridine and 2-(1-hydroxy-4,5-dimethyl-1H-imidazol-2-yl)pyridine, Russ. J. Gen. Chem. 82 (2012) 1859.

[28] C.K. Lee, M.J. Ling, I.J.B. Lin, Organic-inorganic hybrids of imidazole complexes of palladium(II), copper(II) and Zn(II), Cryst. Liq. Cryst. Dalton Trans (2003) 4731.

[29] O. Karagiaridi, W. Bury, A.A. Sarjeant, C.L. Stern, O.K. Farha, J.T. Hupp, Synthesis and characterization of isostructural cadmium zeolitic imidazolate frameworks via solvent-assisted linker exchange, Chem. Sci. 3 (2012) 3256.

[30] P.K. Bhharadwaj, H.J. Schugar, J.A. Potenza, Structure of copper(II)-doped dichlorobis(1,2-dimethylimidazole)zinc(II), Acta Cryst. C47 (1991) 754.

[31] C. Place, J.L. Zimmermann, E. Mulliez, G. Guillot, C. Bois, J.C. Chottard, Crystallographic, electrochemical, and pulsed EPR Study of copper(II) poly-imidazole complexes relevant to the metal sites of copper proteins, Inorg. Chem. 37 (1998) 4030.

[32] J.J. McKinnon, D. Jayatilaka, M.A. Spackman, Towards quantitative analysis of intermolecular interactions with Hirshfeld surfaces, Chem. Comm. 10 (2007) 3814—3816.

[33] M.A. Spackman, D. Jayatilaka, Hirshfeld surface analysis, CrystEngComm 11 (2009) 19—32.

[34] M.A. Spackman, Molecules in crystals, Phys. Scr 87 (2013) 048103.

[35] J.J. McKinnon, M.A. Spackman, A.S. Mitchell, Novel tools for visualizing and exploring intermolecular interactions in molecular crystals, Acta Crystallogr. 60B (2004) 627—668.

[36] N. Shamsudin, A. Ling Tan, D.J. Young, M.M. Jotani, A. Otero-de-la-Rozad, E.R.T. Tiekink, 4-[(1-Benzyl-1H-1,2,3-triazol-4-yl)methoxy]-benzene-1,2-dicarbonitrile: crystal structure, Hirshfeld surface analysis and energy-minimization Calculations, Acta Cryst. E72 (2016) 563—569.

[37] M.A. Spackman, J.J. McKinnon, D. Jayatilaka, Electrostatic potentials mapped on Hirshfeld surfaces provide direct insight into intermolecular interactions in crystals, CrystEngComm 10 (2008) 377—388.

[38] S.M. Kumar, B.C. Manjunath, G.S. Lingaraju, M.M.M. Abdoh, M.P. Sadashiva, N.K. Lokanath, A Hirshfeld surface analysis and crystal structure of 2'-[1-(2-Fluoro-Phenyl)-1H-tetrazol-5-Yl]-4-Methoxy-Biphenyl-2-Carbaldehyde, Cryst. Struct. Theo. Appl. 2 (2013) 124—131.

[39] P. Coppens, X-ray Charge Density and Chemical Bonding, Oxford University press, 1997.

[40] T. Clark, M. Hennemann, J. S. Murray and P. Politzer, Halogen bonding: the sigma-hole. Proceedings of "Modeling interactions in biomolecules II", Prague, September 5th-9th, 2005, J. Mol. Model. 13 (2007) 291—296.

[41] P. Politzer, P. Lane, M.C. Concha, Y.G. Ma, J.S. Murray, An overview of halogen bonding, J. Mol. Model 13 (2007) 305—311.

[42] P. Politzer, J.S. Murray, T. Clark, Halogen bonding: an electrostatically-driven highly directional noncovalent interaction, Phys. Chem. Chem. Phys. 12 (2010) 7748—7757.

[43] Q. Zhao, D. Feng, Influence of transition metals on halogen-bonded complexes of MCCBr···NCH and HCCBr···NCM' (M, M' = Cu, Ag, and Au), J. Mol. Model 19 (2013) 1267—1271.

[44] CrysAlisPro, Oxford Diffraction Ltd., Version 1.171.33.48 (release 15-09-2009 CrysAlis171.NET).

[45] G.M. Sheldrick, A short history of SHELX, Acta Crystallogr. A64 (2008) 112—122.

[46] L. Farrugia, WinGX and ORTEP for Windows: an update, J. Appl. Crystallogr. 4 (2012) 849—854.

[47] A. Spek, Structure validation in chemical crystallography, Acta Crystallogr. D65 (2009) 148—155.

[48] L. Farrugia, ORTEP-3 for Windows - a version of ORTEP-iii with a graphical user interface (GUI), J. Appl. Crystallogr. 30 (1997) 565.

[49] C.F. Macrae, I.J. Bruno, J.A. Chisholm, P.R. Edgington, P. McCabe, E. Pidcock, L. Rodriguez Monge, R. Taylor, J. van de Streek, P.A. Wood, Mercury CSD 2.0 — new features for the visualization and investigation of crystal structures, J. Appl. Crystallogr. 41 (2008) 466—470.

[50] S.K. Wolff, D.J. Grimwood, J.J. McKinnon, M.J. Turner, D. Jayatilaka, M.A. Spackman, CrystalExplorer (Version 3.0), University of Western Australia, 2012.

[51] D. Jayatilaka, D.J. Grimwood, A. Lee, A. Lemay, A.J. Russel, C. Taylor, S.K. Wolff, P. Cassam-Chenai, A. Whitton, TONTO — a System for Computational Chemistry, 2005.

[52] G.S. SüheylaKürkçüoğlu, F.C. Kiraz, E. Sayin, Vibrational spectra, powder X-ray diffractions and physical properties of cyanide complexes with 1-ethylimidazole, Spectrochim. Acta A 149 (2015) 8.

[53] E. Sayın Güneş, S. Kürkçüoğlu, O. Zafer Yeşilel, T. Hökelek, Synthesis, crystal structure and spectroscopic properties of one-dimensional zinc(II)—cyanide complex with 1-methylimidazole, [Zn(μ-CN)(CN)(1-meim)]ₙ, Z. für Kristallogr. - Cryst. Mater. 230 (2015) 421—426.

[54] N. Erici, Z. Kantarci, S. Akyuz, An infrared and raman spectroscopic study of pyrazinecadmium (II) tetracyanometalate (II) Benzene (1/1) clathrates: Cd(C₄H₄N₂)Cd(CN)₄·C₆H₆ and Cd(C₄H₄N₂)Hg(CN)₄·C₆H₆, J. Inclus. Phenom. Mol. 10 (1991) 9.

[55] S. Suzuki, W.J. Orville-Thomas, Molecular force field of pyridine and its application to pyridine-metal complexes Original Research Article, J. Mol. Struct. 37 (1977) 321.

[56] R. López-Garzón, M.D. Gutiérrez-Valero, M.L. Godino-Salido, A. Sanchez-Rodrigo, M. Nogueras-Montiel, J.M. Moreno, R. Odedra, Kh.A.M. El-Bayouki, Synthesis and characterization of Zn(II), Cd(II) and Hg(II) complexes with imidazole derivatives. Crystal structure of dichloro-bis(5-amino-4-carboethoxy-1-p-methoxyphenyl-imidazole)zinc(II), Inorg. Chim. Acta 258 (1997) 33.

[57] Y. Song, D. Hu, F. Liu, Fabrication of fluorescent SiO2@zeolitic imidazolate framework-8 nanosensor for Cu(2+) detection, in: S. Chen, L. Wang (Eds.), Analyst vol. 140, 2015, p. 623.

[58] Y. Zhou, W.X. Mingyan, A. Lan, L. Zhang, R. Feng, F. Liang, M. Hong, Topological and luminescent properties of two coordination polymers constructed from 3-pyridinepropionic acid, Inorg. Chem. Commun. 15 (2012) 140.

[59] K.L. Wong, G.L. Law, Y.Y. Yang, W.T. Wong, Tb(III) postsynthetic functional coordination polymer coatings on ZnO micronanoarrays and their application in small molecule sensing, Adv. Mater 18 (2006) 1051.

[60] (a) C.A. Hunter, Meldola Lecture. The role of aromatic interactions in molecular recognition, Chem. Soc. Rev. 23 (1994) 101–109;
(b) T. Dorn, C. Janiak, K. Abu-Shandi, Hydrogen-bonding, π-stacking and Cl⁻-anion−π interactions of linear bipyridinium cations with phosphate, chloride and [CoCl₄]²⁻ anions, CrystEngComm. 7 (2005) 633–641;
(c) A. Saeed, S. Ashraf, U. Flörke, Z. Y Delgado Espinoza, M. F Erben and H. Pérez, Supramolecular self-assembly of a coumarine-based acylthiourea synthon directed by π-stacking interactions: crystal structure and Hirshfeld surface analysis, J. Mol. Struct., 1111(2016) 76–83.

[61] S.K. Seth, D. Sarkar, A. Roy, T. Kar, Use of π−π forces to steer the assembly of chromone derivatives into hydrogen bonded supramolecular layers: crystal structures and Hirshfeld surface analyses, CrystEngComm 13 (2011) 4528–4535.

[62] S.K. Seth, Discrete cubic water cluster: an unusual building block of 3D supramolecular network, Inorg. Chem. Commun. 43 (2014) 60–63.

[63] S. Soudani, V. Ferretti, C. Jelsch, F. Lefebvre, C. Ben Nasr, Synthesis, structural characterization, Hirshfeld surface analysis and spectroscopic studies of cadmium (II) chloride complex with 4-hydroxy-1-methylpiperidine, J. Solid State Chem. 237 (2016) 7–13.

[64] P. Manna, S.K. Seth, A. Das, J. Hemming, R. Prendergast, M. Helliwell, S.R. Choudhury, A. Frontera, S. Mukhopadhyay, Anion induced formation of supramolecular associations involving lone pair−π and Anion−π interactions in Co(II) malonate complexes: experimental observations, Hirshfeld surface analyses and DFT studies, Inorg. Chem. 51 (2012) 3557–3571.

[65] P. Panini, T.P. Mohan, U. Gangwar, R. Sankolli, D. Chopra, Quantitative crystal structure analysis of 1,3,4-thiadiazole derivatives, CrystEngComm 15 (2013) 4549–4564.

[66] M. Pourayoubi, S.S. Bayraq, A. Tarahhomi, M. Necas, K. Fejfarová, M. Dusek, Hirshfeld surface analysis of new organotin(IV)-phosphoramide complexes, J. Organomet. Chem. 751 (2014) 508–518.

[67] M.A. Spackman, Molecular electric moments from x-ray diffraction data, Chem. Rev. 92 (1992) 1769–1797.

[68] M.A. Spackman, J.J. McKinnon, D. Jayatilaka, Electrostatic potentials mapped on Hirshfeld surfaces provide direct insight into intermolecular interactions in crystals, CrystEngComm 10 (2008) 377–388.

[69] J.J.P. Stewart, MOPAC2016, Version 16.125W, Stewart Computational Chemistry, Colorado Springs, CO, USA, http://OpenMOPAC.net.